

Fabrication and investigation of ferroelectric memristorswith various synaptic plasticities

Qi Qin(秦琦), Miaocheng Zhang(张缪城), Suhao Yao(姚苏昊), Xingyu Chen(陈星宇), Aoze Han(韩翱泽),Ziyang Chen(陈子洋), Chenxi Ma(马晨曦), Min Wang(王敏), Xintong Chen(陈昕彤), Yu Wang(王宇),Qiangqiang Zhang(张强强), Xiaoyan Liu(刘晓燕), Ertao Hu(胡二涛), Lei Wang(王磊), and Yi Tong(童祎)
Citation: Chin. Phys. B, 2022, 31 (**7**): 078502. DOI: 10.1088/1674-1056/ac3ece
Journal homepage: http://cpb.iphy.ac.cn; http://iopscience.iop.org/cpb

What follows is a list of articles you may be interested in

Analysis of the generation mechanism of the S-shaped *J*—*V* curves of MoS_2/Si-based solar cells

He-Ju Xu(许贺菊), Li-Tao Xin(辛利桃), Dong-Qiang Chen(陈东强), Ri-Dong Cong(丛日东), and Wei Yu(于威)
Chin. Phys. B, 2022, 31 (**3**): 038503. DOI: 10.1088/1674-1056/ac1b80

Trigger mechanism of PDSOI NMOS devices for ESD protection operating under elevated temperatures

Jia-Xin Wang(王加鑫), Xiao-Jing Li(李晓静), Fa-Zhan Zhao(赵发展), Chuan-Bin Zeng(曾传滨), Duo-Li Li(李多力), Lin-Chun Gao(高林春), Jiang-Jiang Li(李江江), Bo Li(李博), Zheng-Sheng Han(韩郑生), and Jia-Jun Luo(罗家俊)
Chin. Phys. B, 2021, 30 (**7**): 078501. DOI: 10.1088/1674-1056/abe2fe

Characteristics and mechanisms of subthreshold voltage hysteresis in 4H-SiC MOSFETs

Xi-Ming Chen(陈喜明), Bang-Bing Shi(石帮兵), Xuan Li(李轩), Huai-Yun Fan(范怀云), Chen-Zhan Li(李诚瞻), Xiao-Chuan Deng(邓小川), Hai-Hui Luo(罗海辉), Yu-Dong Wu(吴煜东), and Bo Zhang(张波)
Chin. Phys. B, 2021, 30 (**4**): 048504. DOI: 10.1088/1674-1056/abd391

Negative photoconductivity in low-dimensional materials

Boyao Cui(崔博垚), Yanhui Xing(邢艳辉), Jun Han(韩军), Weiming Lv(吕伟明), Wenxing Lv(吕文星), Ting Lei(雷挺), Yao Zhang(张尧), Haixin Ma(马海鑫), Zhongming Zeng(曾中明), and Baoshun Zhang(张宝顺)
Chin. Phys. B, 2021, 30 (**2**): 028507. DOI: 10.1088/1674-1056/abcf41

An improved memristor model for brain-inspired computing

Errui Zhou(周二瑞), Liang Fang(方粮), Rulin Liu(刘汝霖), Zhenseng Tang(汤振森)
Chin. Phys. B, 2017, 26 (**11**): 118502. DOI: 10.1088/1674-1056/26/11/118502

Fabrication and investigation of ferroelectric memristors with various synaptic plasticities

Qi Qin(秦琦)[1], Miaocheng Zhang(张缪城)[1,†], Suhao Yao(姚苏昊)[1], Xingyu Chen(陈星宇)[1], Aoze Han(韩翱泽)[1], Ziyang Chen(陈子洋)[1], Chenxi Ma(马晨曦)[2], Min Wang(王敏)[1], Xintong Chen(陈昕彤)[1], Yu Wang(王宇)[1], Qiangqiang Zhang(张强强)[1], Xiaoyan Liu(刘晓燕)[1], Ertao Hu(胡二涛)[1], Lei Wang(王磊)[1,‡], and Yi Tong(童祎)[1,§]

[1] *College of Electronic and Optical Engineering and College of Microelectronics, Nanjing University of Posts and Telecommunications, Nanjing* 210023, *China*
[2] *Key Laboratory for Organic Electronics and Information Displays and Jiangsu Key Laboratory for Biosensors, Nanjing University of Posts and Telecommunications, Nanjing* 210023, *China*

(Received 13 September 2021; revised manuscript received 5 November 2021; accepted manuscript online 1 December 2021)

In the post-Moore era, neuromorphic computing has been mainly focused on breaking the von Neumann bottlenecks. Memristors have been proposed as a key part of neuromorphic computing architectures, and can be used to emulate the synaptic plasticities of the human brain. Ferroelectric memristors represent a breakthrough for memristive devices on account of their reliable nonvolatile storage, low write/read latency and tunable conductive states. However, among the reported ferroelectric memristors, the mechanisms of resistive switching are still under debate. In addition, there needs to be more research on emulation of the brain synapses using ferroelectric memristors. Herein, Cu/$PbZr_{0.52}Ti_{0.48}O_3$ (PZT)/Pt ferroelectric memristors have been fabricated. The devices are able to realize the transformation from threshold switching behavior to resistive switching behavior. The synaptic plasticities, including excitatory post-synaptic current, paired-pulse facilitation, paired-pulse depression and spike time-dependent plasticity, have been mimicked by the PZT devices. Furthermore, the mechanisms of PZT devices have been investigated by first-principles calculations based on the interface barrier and conductive filament models. This work may contribute to the application of ferroelectric memristors in neuromorphic computing systems.

Keywords: brain-inspired computing, ferroelectric memristors, mechanisms, resistive-switching

PACS: 85.35.–p, 87.19.lv **DOI:** 10.1088/1674-1056/ac3ece

1. Introduction

The development of artificial intelligence is currently hindered by the bottlenecks of traditional von Neumann computing systems. The human brain, which can perform parallel operation and realize computing-in-memory, provides a solution to break the von Neumann bottlenecks.[1–3] Memristive devices feature continuously tunable conductive states, specific structures similar to the synapses in human brain, as well as excellent performance in emulating various synaptic plasticities. As a result, they are being explored to improve the power consumption, integration and efficiency of neuromorphic computing systems.[4–10]

Recently, ferroelectric memristors have attracted huge attention for realizing non-volatile storage due to their great endurance, stable conductive states, fast switching speed and enormous application potential in microelectronics.[11–18] The polarization of ferroelectric tunnel junctions (FTJs) promotes charge accumulation and FTJs can be modified by variation of the interface barrier,[16] which will enhance the performance of memristive devices. Nevertheless, applications of ferroelectric memristive devices in artificial synapses have been rarely explored. In addition, the specific mechanisms of memristors with FTJs have not been fully clarified.[17,18] Therefore, the emulation of various synaptic functions and conductive mechanisms of ferroelectric memristors need to be investigated in detail.

Herein, Cu/$PbZr_{0.52}Ti_{0.48}O_3$ (PZT)/Pt memristors have been fabricated by the traditional process for fabricating semiconductor devices. Physical characterizations of the PZT devices have been done using atomic force microscopy (AFM), scanning electron microscopy (SEM) and piezo-response force microscopy (PFM). During the electrical measurements, the transition from unipolar threshold-switching behavior to bipolar resistive-switching behavior (R_{off}/R_{on} 10^4, switching voltage 3.5 V) can be observed by the modulation of the external signals. The switching mechanisms of the PZT devices based on interface barrier and conductive filament models have been studied in detail. Moreover, upon the stimulation of continuous pulses of voltage, some biological phenomena have been mimicked.[19–25] Therefore, this work may create more opportunities for the application of ferroelectric memristors in neuromorphic computing systems.

2. Devices and experiments

The structure of the PZT devices is schematically shown in Fig. 1(a). First, a p-type Si wafer was cleaned and used

†Corresponding author. E-mail: zmcstudy@163.com
‡Corresponding author. E-mail: leiwang1980@njupt.edu.cn
§Corresponding author. E-mail: tongyi@njupt.edu.cn

© 2022 Chinese Physical Society and IOP Publishing Ltd

as the substrate. Next, 100 nm Pt was deposited onto the substrate as the bottom electrode by physical vapor deposition (PVD). Finally, 40 nm PZT and 80 nm Cu with a shadow mask, as the ferroelectric film and top electrode, respectively, were successively grown on the Pt layer in the same way. The surface roughness of obtained PZT layer was investigated by AFM (Dimension Icon). The sectional structure of Cu/PZT/Pt memristors was observed by SEM (Hitachi S-4800). Moreover, the ferroelectric properties of PZT film were analyzed by PFM. To investigate the electrical properties of the PZT ferroelectric memristors, a bidirectional scan voltage was applied to the devices (Keithley 4200A SCS Semiconductor Analyzer and Cascade Micromesh M150).

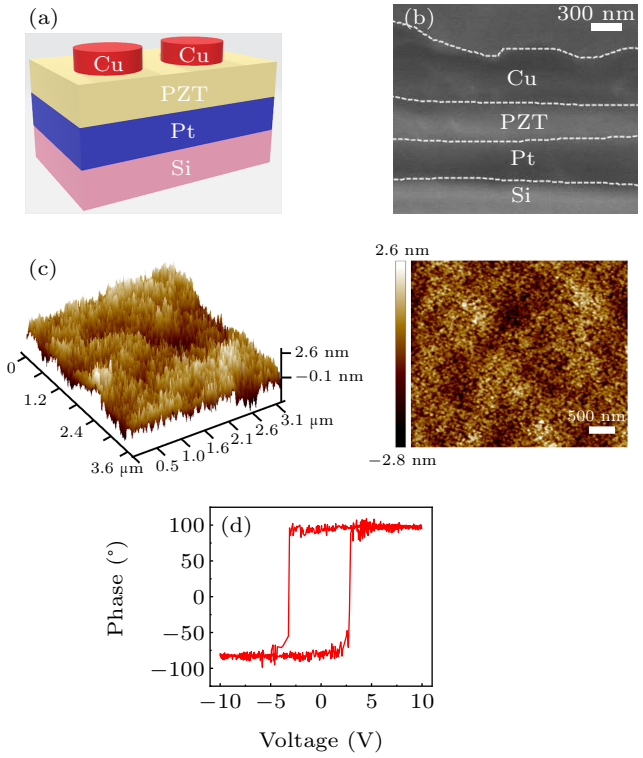


Fig. 1. Physical characterizations of the PZT devices. (a) The structural representation of PZT devices. The SEM (b) and AFM picture (c) of sectional structure. (d) The phase hysteresis curve of the PZT film measured by PFM.

3. Results and discussion

3.1. The physical characterizations

In order to analyze the stability and large-area uniformity of the PZT memristors, the sectional structure was observed by SEM. As shown in Fig. 1(b), the interfaces between each layer were clearly distinguished by white lines (the scale bar is 300 nm). In addition, AFM was performed on the PZT film. The AFM images of the PZT film with a scanning area of 3.6 μm × 3.1 μm and a height range of −2.8 nm to 2.6 nm are shown in Fig. 1(c). The root-mean-square (RMS) roughness of the film is 0.77 nm. It can be observed from the right panel that there are no obvious large dark or light patches. Therefore, the results indicate a smooth surface of the PZT film in a direction perpendicular to the substrate. In addition, the images of the PFM phase measured by the voltage sweep (−10 V to +10 V) are presented in Fig. 1(d). The 180° phase difference suggests that the PZT ferroelectric film exhibits two opposite polarization states during the voltage sweep.

3.2. The switching characteristics

In this work, successive direct current (DC) voltage sweeps with increasing current compliances (from 5×10^{-5} A to 5×10^{-4} A) were applied to the devices. Interestingly, by precise regulation of the current compliances and the ranges of the voltage sweep, the devices can realize the transition of switching characteristics from threshold switching (TS) to resistance switching (RS). The results of the first four voltage sweeps are presented in Fig. 2(a). It can be seen that the devices exhibit TS characteristics at comparatively small current compliances (5×10^{-5} A and 1×10^{-4} A). Meanwhile, the devices exhibit RS characteristics at a comparatively large current compliance (5×10^{-4} A), which can be inferred from Fig. 2(b). The transition of switching characteristics can be explained using the conductive filaments model. Larger ranges of voltage sweep and current compliances will result in bigger conductive filaments. The realization of tuning the devices from volatile storage to nonvolatile storage may offer more possibilities for applications.

The typical current–voltage curve of PZT devices is presented in Fig. 2(c). During the positive voltage sweep, a rapid increase in current occurred at approximately 3.5 V, corresponding to the 'SET' process. During the negative voltage sweeps, the 'RESET' process can be also observed at −3.5 V. The data from the retention test at high- and low-resistance states (HRS and LRS) are displayed in Fig. 2(d), read at 0.02 V. It can be observed that the switching ratio R_{off}/R_{on} is approximately 10^4. There is no noticeable change in the two resistance states in 4000 s. In order to evaluate the repeatability of the Cu/PZT/Pt devices, consecutive DC voltage sweeps were applied to the devices. The cumulative distribution of R_{on} and R_{off} for 50 cycles is shown in Fig. 2(e). The HRS and LRS can be easily distinguished from the window and the conformity of each state is at an acceptable level. As a result, the devices exhibit repeatable bipolar switching characteristics with a high switching ratio of 10^4, a low operating voltage of ±3.5 V and a long retention time of over 4000 s.

3.3. The simulation of synaptic behaviors

The bipolar analogous characteristics of the PZT devices were further investigated. As shown in Figs. 3(a) and 3(b), the response current increases regularly under positive voltage scans. Similarly, the response current decreases continuously under successive negative voltage scans. These results confirm that the devices exhibit excellent analogous switching characteristics under both positive and negative voltage sweeps.[27] This will make it possible to mimic synaptic behaviors using these ferroelectric memristors.

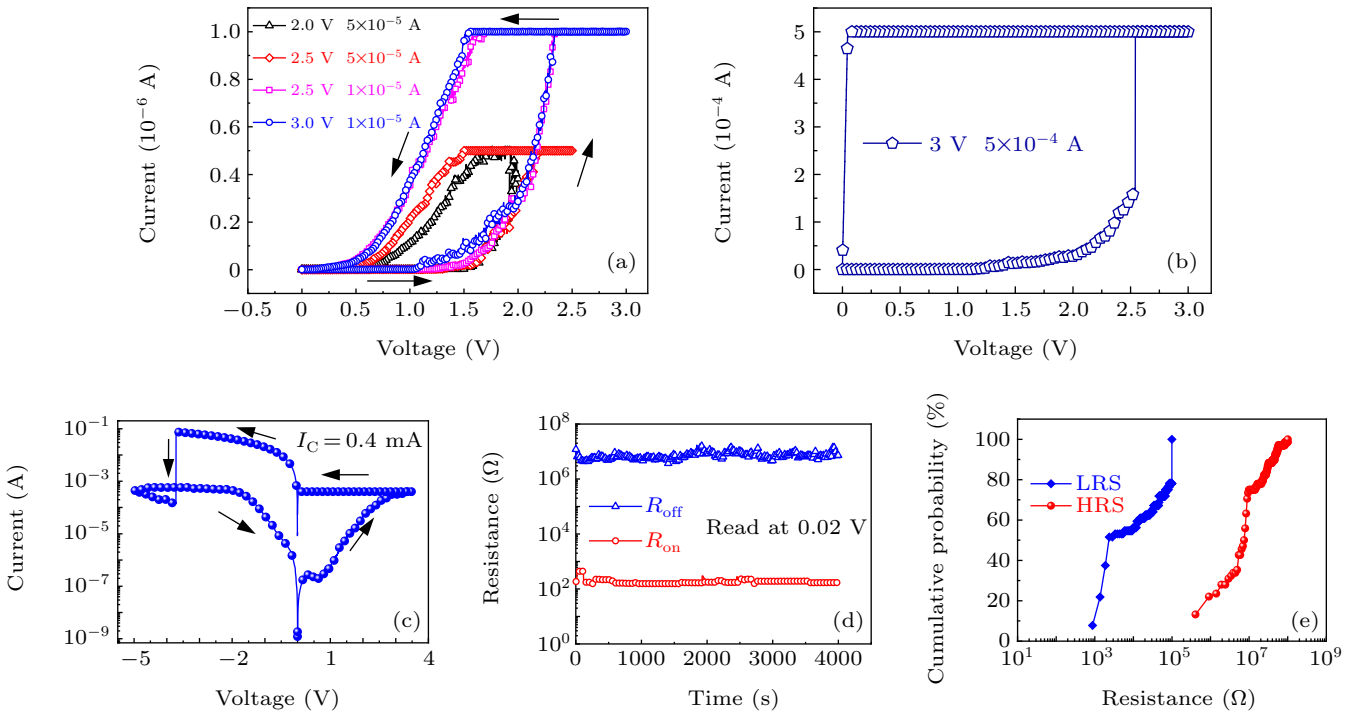


Fig. 2. Electrical characteristics of PZT memristors. The transition from volatile storage (a) to nonvolatile storage (b) by changing the ranges of voltage sweep and current compliances. The ranges of voltage sweep and current compliances have been indicated. (c) The bipolar resistive-switching characteristics. (d) The memory retention test, read at 0.02 V. (e) The cumulative probability of high resistance states and low resistance states (extracted at 0.1 V) of Cu/PZT/Pt memristors.

A schematic diagram of the functions of neurons in the human brain is displayed in Fig. 3(c). A biological synapse is the key part where two neurons contact each other by transferring neurotransmitters. Under external stimulation, action potentials from a neuron can be sent to the next neuron(s) via synapses and produce an excitatory post-synaptic current (EPSC).[26,28] As shown in Fig. 3(c), a single voltage pulse (4 V, 200 ms) was imposed on the memristors to mimic this phenomenon. The pulse reached at 450 ms. The post-synaptic current increases rapidly at the same time as the pulse arrives and gradually decays when the pulse is removed, as demonstrated in Fig. 3(c). The variation in conductance is attributed to the formation of conductive filaments in the PZT film. The final value of the response current is larger than that of the initial state, indicating that the generated conductive filaments made of oxygen vacancies do not disappear immediately.

With respect to neuroscience, synaptic plasticity means that the connections between neurons can be adjusted. Paired-pulse facilitation (PPF) and paired-pulse depression (PPD) are typical short-term plasticity processes, which can be simulated using the PZT memristors. The responses of the memristors to two consecutive positive pulses (3 V, 20 ms) are presented in the inset of Fig. 3(d). The conductance of devices increases when the second pulse arrives, showing that the devices are more sensitive to the second pulse.[29–31] Moreover, the PPF index is related to the inter-spike interval, which is displayed in Fig. 3(d). The functional relationship is as follows:

$$y = 0.9810 \times \exp(-\Delta t/36.63) + 0.1679. \quad (1)$$

Thus, the PPF-related short-term synaptic plasticity has been simulated using PZT ferroelectric memristors.

In a biological synapse, the variation from potentiation to depression of the synapse can be caused by the application of continuous spikes with the same interval. This synaptic function can be demonstrated using the PZT memristors. In Fig. 3(e), under a train of pulses (3 V, 20 ms) with intervals of 100 ms, the response current rises constantly and reaches a saturation state. The current gradually decays after 130 pulses, revealing that the transition from PPF to PPD behavior has occurred. The PPF behavior was induced by the movement of oxygen vacancies. However, when the current saturates at a high level, the back-diffusion of oxygen vacancies induced by a higher concentration gradient is inevitable. The conductive filaments are not stable, causing the decrease in current.

The spike timing-dependent plasticity (STDP) rule is a vital supplement to the Hebbian learning rule, revealing that the connection between neurons can be modified according to the sequence of pre- and post-neuron spikes.[32] In order to implement the STDP function, a pulse pair was applied to the PZT devices. The pulse protocol and results are demonstrated in Fig. 3(f). Here, Δt refers to the time interval between two pulses

$$\Delta t = t_{\text{post}} - t_{\text{pre}}, \quad (2)$$

and ΔW is the rate of change of conductance

$$\Delta W = (G_2 - G_1)/G_1, \quad (3)$$

where G_1 and G_2 are the conductances measured before and

after the application of pulses, respectively. It can be observed that if pre-neuron pulse precedes the post-neuron pulse ($\Delta t > 0$), the connection between neurons will be enhanced ($\Delta W > 0$). When the order of pulses is reversed ($\Delta t < 0$), the conductance decreases ($\Delta W < 0$), corresponding to a depressed connection between neurons. These results have demonstrated that the STDP learning rule has been mimicked using the PZT devices.[33,34]

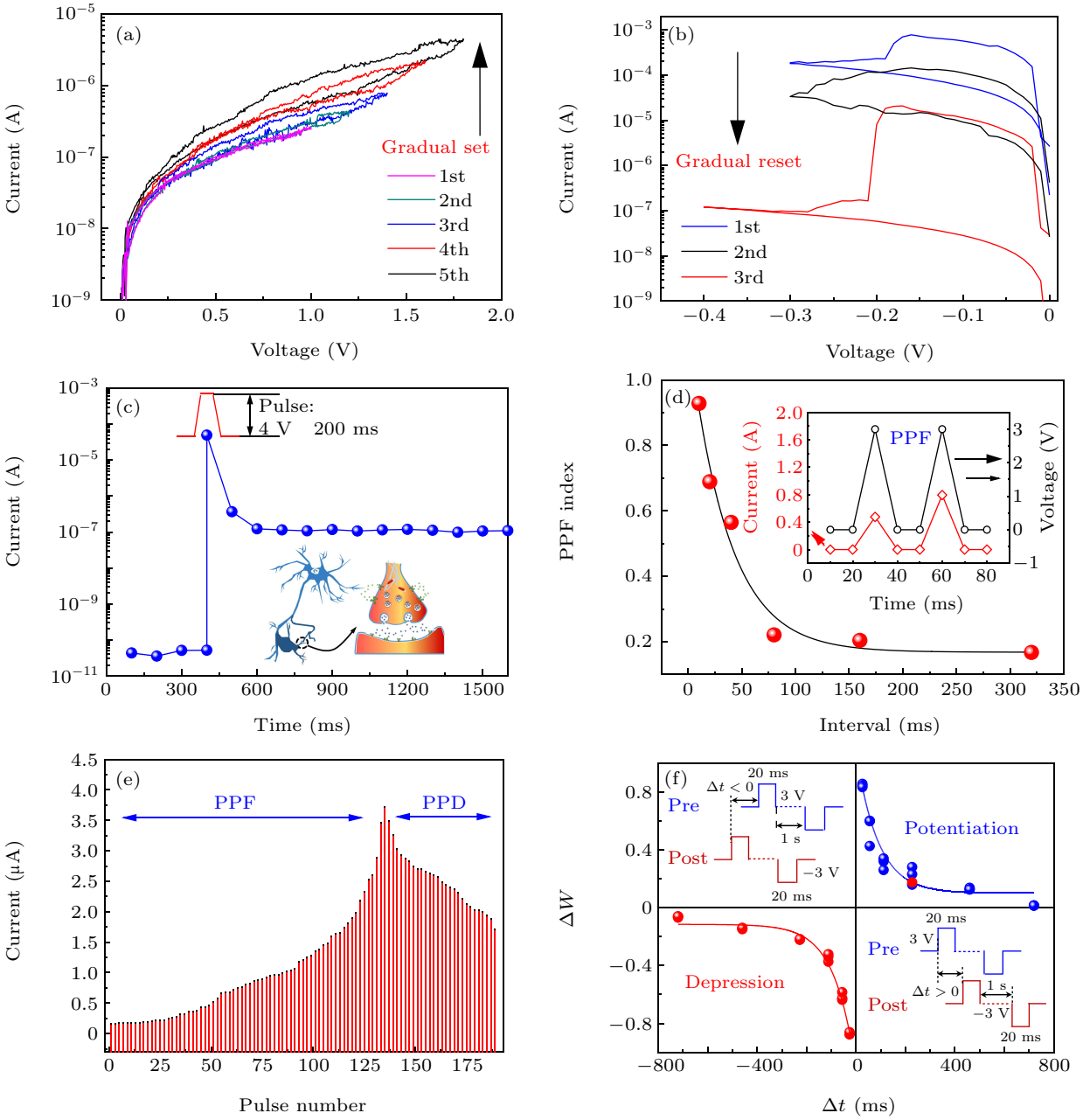


Fig. 3. The emulation of synaptic plasticities by PZT memristors. (a) The analogy behaviors under positive voltage sweeps. (b) The analogy behaviors under negative voltage sweeps. (c) EPSC responses under a pulse signal (4 V, 200 ms). The inset displays the functions of neurons and synapses of human brain. (d) The fitting map of relationship between PPF index and pulse interval. The PPF index is calculated as $(I_2 - I_1)/I_1$, in which I_2 and I_1 are the peak values of the second and first post-synaptic current responses. (e) The inflection from PPF behavior to PPD behavior. (f) The presentation of pulse protocol and simulation of STDP function.

3.4. The conductive mechanisms

To better understand the switching process of the PZT memristors, first-principles calculations were performed to investigate the conductive mechanisms of the devices. First, the $PbTiO_3$ crystal structure with the number 236933 and space group *P*4*mm* was selected from the Inorganic Crystal Structure Database. After optimization, the parameters of the unit cell were $a = 4.01$ Å, $b = 4.01$ Å, $c = 4.20$ Å and the optimized structure was expanded to $3 \times 3 \times 3$. The structure obtained consisted of 27 Ti atoms, 14 of which were replaced with Zr atoms. The one with the lowest energy from the 10 crystal structures was chosen and the cleaved (100) surface was optimized. The dipole moment was eliminated by balancing the interfaces on both sides of the vacuum layer. Based on the final

structure, the work function of PZT was calculated as 4.52 eV. Additionally, in order to work out the migration barrier of Cu ions and oxygen vacancies in the PZT layer, the two structures were doped with Cu atoms and oxygen vacancies, respectively. The structures were optimized and five points were analyzed between the initial and final states (Figs. 4(a) and 4(b)). Finally, the migration barrier of oxygen (0.44357 eV) is far less than that of Cu atoms (1.651064 eV), indicating that it is easier for oxygen vacancies to migrate in the PZT layer than Cu ions. As a result, the migration of Cu ions was ignored in the following.

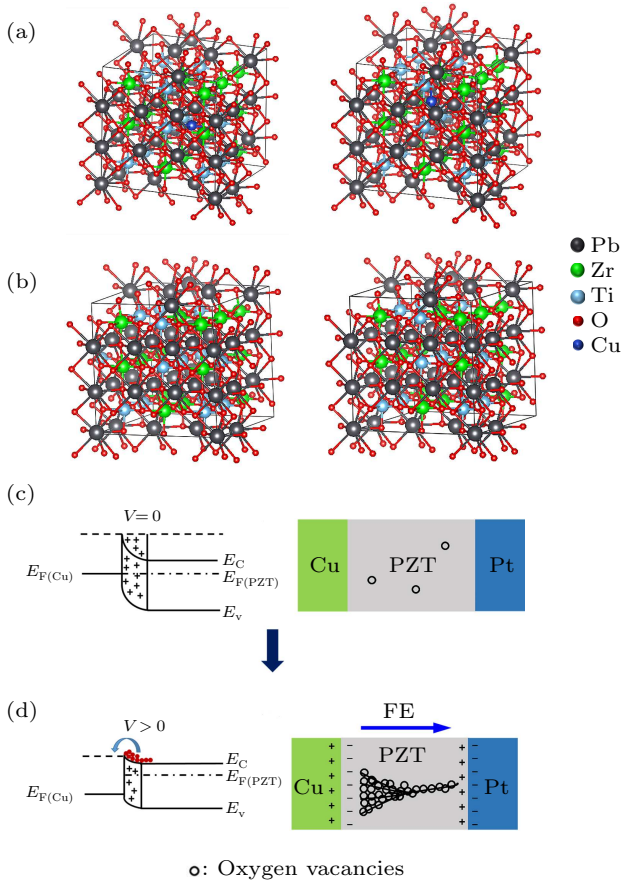


Fig. 4. The internal mechanisms of PZT devices based on first-principles calculation. The Cu-doped (a) and oxygen vacancies-doped (b) PZT structure for calculation of migration barrier. The initial and final state of migration have been indicated. The variation of interface barrier and migration of oxygen vacancies under different voltage bias, including the HRS (c) and LRS (d). The polarization states have been indicated by the blue arrows.

Schematic diagrams of possible conductive mechanisms of the Cu/PZT/Pt devices are shown in Fig. 4. The external voltages were applied to the Cu layer. Since the work function of Cu (4.65 eV) is larger than that of n-type PZT (4.52 eV),[35] there is a barrier at the interface of the Cu and PZT and positive charges in the depletion layer, indicating the initial state of the FTJ ($V = 0$).[12,13] Several oxygen vacancies already exist in the PZT film. Upon a positive voltage bias ($V > 0$), the Cu layer is oxidized to CuO_x and more oxygen vacancies appear in the PZT layer.[36] Meanwhile, the polarization is pointing to the Pt layer and the negatively polarized charges tend to suppress the interface barrier of the PZT layer,[37] leading to the transport of electrons from the PZT layer to the Cu layer. As a result, the connection of conductive filaments made of oxygen vacancies and suppression of the interface barrier both contribute to state switching. On the contrary, under a negative bias, the interface barrier of the PZT layer may be enhanced by the positively polarized charges. The disruption of conductive filaments is induced by the migration of the oxygen vacancies in the opposite direction. Thus, the devices are switched to HRS.[38] Therefore, the excellent performances of the devices can be explained. The migration of oxygen vacancies and the variation of interface barriers both contribute to the state switching of PZT memristors.

4. Conclusion and perspectives

In summary, ferroelectric memristors based on PZT tunnel junctions have been manufactured. The hysteresis curves were measured by the Cu/PZT/Pt devices. The transition from threshold-switching behavior to resistive-switching behavior has been observed. Furthermore, the conduction mechanisms based on the interface barrier and oxygen vacancies of the PZT devices have been researched in detail. Additionally, under continuous voltage pulses, the memristors are able to simulate biological synaptic responses, including analogous behaviors and synaptic plasticities. This work may contribute to the developments of future neuromorphic computing.

Acknowledgments

Project supported by Jiangsu Province Research Foundation (Grant Nos. BK20191202, RK106STP18003, and SZDG2018007), the Jiangsu Province Research Foundation (Grant Nos. BK20191202, RK106STP18003, and SZDG2018007), the Research Innovation Program for College Graduates of Jiangsu Province (Grant Nos. KYCX20_0806, KYCX19_0960, and SJCX19_0268), and NJUPTSF (Grant Nos. NY217116, NY220078, and NY218107).

References

[1] Gang D, Dou M L, Liu R Y and Guo M 2021 *Chin. Phys. B* **30** 078401
[2] Liu B, Liu Z, Chiu I S, Di M, Wu Y, Wang J C, Hou T H and Lai C S 2018 *ACS Appl. Mater. Interfaces* **10** 20237
[3] Lu K, Li Y, He W, Chen J, Zhou Y, Duan N, Jin M, Gu W, Xue K, Sun H and Miao X 2018 *Appl. Phys. A* **124** 438
[4] Wang Z, Yin M, Zhang T, Cai Y, Wang Y, Yang Y and Huang R 2016 *Nanoscale* **8** 14015
[5] Boppidi P K R, Suresh B, Zhussupbekova A, Biswas P, Mullarkey D, Raj P M P, Shvets I V and Kundu S 2020 *IEEE Trans. Electron. Dev.* **67** 3451
[6] Xia Q and Yang J J 2019 *Nat. Mater.* **18** 309
[7] Yan X, Zhao Q, Chen A P, Zhao J, Zhou Z, Wang J, Wang H, Zhang L, Li X, Xiao Z, Wang K, Qin C, Wang G, Pei Y, Li H, Ren D, Chen J and Liu Q 2019 *Small* **15** 1901423
[8] Zhang X, Liu S, Zhao X, Wu F, Wu Q, Wang W, Cao R, Fang Y, Lv H, Long S, Liu Q and Liu M 2017 *IEEE Electron Dev. Lett.* **38** 1208
[9] Lian X, Shen X, Zhang M, Xu J, Gao F, Wan X, Hu E, Guo Y, Zhao J and Tong Y 2019 *Appl. Phys. Lett.* **115** 063501

[10] Guo Y B and Zhu L Q 2020 *Chin. Phys. B* **29** 078502
[11] Gabel M and Gu Y 2020 *Adv. Funct. Mater.* **31** 2009999
[12] Chanthbouala A, Garcia V, Cherifi R O, Bouzehouane K, Fusil S, Moya X, Xavier S, Yamada H, Deranlot C, Mathur N D, Bibes M, Barthelemy A and Grollier J 2012 *Nat. Mater.* **11** 860
[13] Hu Z, Qian Li, Li M, Wang Q, Zhu Y, Liu X, Zhao X, Liu Y and Dong S 2013 *Appl. Phys. Lett.* **102** 102901
[14] Li J, Ge C, Du J, Wang C, Yang G and Jin K 2020 *Adv. Mater.* **32** 1905764
[15] Ma C, Luo Z, Huang W, Zhao L, Chen Q, Lin Y, Liu X, Chen Z, Liu C, Sun H, Jin X, Yin Y and Li X 2020 *Nat. Commun.* **11** 1439
[16] Majumdar S, Tan H, Pande I and Dijken S 2019 *Adv. Electron. Mater.* **7** 091114
[17] Sun H, Luo Z, Zhao L, Liu C, Ma C, Lin Y, Gao G, Chen Z, Bao Z, Jin X, Yin Y and Li X 2020 *ACS Appl. Electron. Mater.* **2** 1081
[18] Yan Z, Yau H, Li Z, Gao X, Dai J and Liu J M 2016 *Appl. Phys. Lett.* **109** 053506
[19] Fu T, Liu X, Gao H, Ward J E, Liu X, Yin B, Wang Z, Zhuo Y, Walker D J F, Yang J J, Chen J, Lovley D R and Yao J 2020 *Nat. Commun.* **11** 1861
[20] Yan X, Zhao J, Liu S, Zhou Z, Liu Q, Chen J and Liu X 2018 *Adv. Funct. Mater.* **31** 265202
[21] Wang Z, Zeng T, Ren Y, Lin Y, Xu H, Zhao X, Liu Y and Ielmini D 2020 *Nat. Commun.* **11** 1510
[22] Krishnaprasad A, Choudhary N, Das S, Dev D, Kalita H, Chung H S, Aina O, Jung Y and Roy T 2019 *Appl. Phys. Lett.* **115** 103104
[23] Zhou L, Yang S, Ding G, Yang J Q, Ren Y, Zhang S R, Mao J Y, Yang Y, Zhou Y and Han S T 2019 *Nano Energy* **58** 293
[24] Zhao J, Zhou Z, Zhang Y, Wang J, Zhang L, Li X, Zhao M, Wang H, Pei Y, Zhao Q, Xiao Z, Wang K, Qin C, Wang G, Li H, Ding B, Yan F, Wang K, Ren D, Liu B and Yan X 2018 *J. Mater. Chem. C* **7** 1298
[25] Zhao Y, Zhang J, Wang Y and Chen Z 2020 *Nanoscale Res. Lett.* **15** 1
[26] Lee T H, Hwang H G, Woo J U, Kim D H, Kim T W and Nahm S 2018 *ACS Appl. Mater. Interfaces* **10** 25673
[27] Sun Y, Xu H, Liu S, Song B, Liu H, Liu Q and Li Q 2018 *IEEE Electron. Dev. Lett.* **39** 492
[28] Hwang H G, Woo J U, Lee T H, Park S M, Lee T G, Lee W H and Nahm S 2019 *Mater. Des.* **187** 108400
[29] Lee M J, Han S, Jeon S H, Park B H, Kang B S, Ahn S E, Kim K H, Lee C B, Kim C J, Yoo I K, Seo D H, Li X S, Park J B, Lee J H and Park Y 2009 *Nano Lett.* **9** 1476
[30] Yan X, Zhao J, Liu S, Zhou Z, Liu Q, Chen J and Liu X 2018 *Adv. Funct. Mater.* **28** 1705320
[31] Yan X, Zhou Z, Zhao J, Liu Q, Wang H, Yuan G and Chen J 2018 *Nano Res.* **11** 1183
[32] Panwar N, Rajendran B and Ganguly U 2017 *IEEE Electron Dev. Lett.* **38** 740
[33] Kim M K and Lee J S 2018 *ACS Nano* **12** 1680
[34] Sun J, Wang H, Wang Z, Song F, Zhu Q, Dang B, Gao H, Yang M, Ma X and Hao Y 2019 *IEEE Electron Dev. Lett.* **40** 706
[35] Zhang K, Meng D, Bai F, Zhai J and Wang Z L 2020 *Adv. Funct. Mater.* **30** 2002945
[36] Hou P, Zhong X, Wang J and Wu Y 2016 *RSC Adv.* **6** 54113
[37] Ma Z, Li L, Wang Y, Zhou P, Guo Y, Liu Y, Liang K, Qi Y and Zhang T 2020 *Appl. Phys. Lett.* **116** 032903
[38] Molinari A, Witte R, Neelisetty K K, Gorji S, Kübel C, Münch I, Wöhler F, Hahn L, Hengsbach S, Bade K, Hahn H and Kruk R 2020 *Adv. Mater.* **32** 1907541